Journal of Rock Mechanics and Geotechnical Engineering 18 (2026) 3991–4006

Contents lists available at ScienceDirect

Journal of Rock Mechanics and Geotechnical Engineering

journal homepage: www.jrmge.cn

Full Length Article

Impact of physical heterogeneity on hydro-mechanical behaviors in full-scale buffer blocks for HLRW repositories

Wen-Jie Dai [a,b,c], Jing-Li Xie [a,c], Sheng-Fei Cao [a,c], Yong-Gui Chen [b,d,*]

[a] Beijing Research Institute of Uranium Geology, Beijing, 100029, China
[b] Department of Geotechnical Engineering, College of Civil Engineering, Tongji University, Shanghai, 200092, China
[c] CAEA Innovation Center for Geological Disposal of High-Level Radioactive Waste, Beijing, 100029, China
[d] State Key Laboratory of Disaster Reduction in Civil Engineering, Tongji University, Shanghai, 200092, China

ARTICLE INFO

Article history:
Received 9 February 2025
Received in revised form
2 June 2025
Accepted 11 June 2025
Available online 23 August 2025

Keywords:
Full-scale buffer block
Inherent heterogeneity
Physical property
Hydro-mechanical behavior

ABSTRACT

Compacted bentonite blocks are proposed for buffer barriers in deep geological repositories for high-level radioactive waste (HLRW) disposal. These blocks, manufactured through uniaxial compression in molds, exhibit heterogeneity that may impact long-term buffer performance. This study focuses on the physical and hydro-mechanical heterogeneity of full-scale blocks induced by the compaction process. Sector-shaped blocks, with radii of 600 mm and 1200 mm and a height of 200 mm, were axially compressed. Key parameters, including water content, dry density, elasticity modulus, swelling pressure, and permeability, were measured to assess the heterogeneity. Results show that the heterogeneity in the upper layer is primarily caused by differences in drainage and gas expulsion pathways. As depth increases, water content and dry density become more correlated. Hydro-mechanical behavior is largely controlled by dry density, but its fluctuation ratio is much higher than that of dry density. Regarding the microstructure, pore structure heterogeneity follows the order: corner regions > edge regions > center regions, and upper layer > middle layer > lower layer. Vertical microcracks also develop to varying degrees, increasing the anisotropy of the blocks. Upon these observations, the study thoroughly discusses the feasibility and challenges of reckoning the hydro-mechanical properties of blocks using dry density distribution alongside laboratory-scale data. Additionally, it proposes an indicator to evaluate the overall heterogeneity of buffer blocks. These findings highlight the inherent heterogeneity of compacted bentonite blocks at the engineering scale, providing valuable insights for future experiments and simulations.

1. Introduction

The final disposal of high-level radioactive waste (HLRW) is a critical issue for the sustainable development of the nuclear industry and environmental protection (Seiphoori et al., 2014; Asensio et al., 2018; Chen et al., 2019; Ye et al., 2020). Deep geological disposal is the internationally recognized solution, involving the isolation of HLRW within geological formations at depths of 500 m–1000 m (Gao et al., 2023). This approach employs a multi-barrier system comprising engineered and natural barriers to contain and isolate radioactive nuclides effectively (Lee et al., 2016; Cui et al., 2023; Gupta et al., 2023). In a deep geological repository, the engineered barriers consist of waste containers, buffer materials, and backfill materials, while the surrounding host rock serves as a natural barrier to impede the migration of radioactive nuclides (Dai et al., 2024). Buffer materials, typically pre-compacted blocks, surround waste containers, serving as mechanical, hydraulic, and chemical barriers while facilitating the dissipation of heat generated by HLRW (Wang et al., 2014; Dutta and Mishra, 2015; Joseph et al., 2017; Chen et al., 2019). These blocks are commonly manufactured by compressing bentonite powders into high-density shapes of specific dimensions using specialized equipment, playing a critical role in ensuring the long-term safety and stability of the repository. However, the hydro-

* Corresponding author. Department of Geotechnical Engineering, College of Civil Engineering, Tongji University, Shanghai, 200092, China.
E-mail address: cyg@tongji.edu.cn (Y.-G. Chen).

Peer review under responsibility of Institute of Rock and Soil Mechanics, Chinese Academy of Sciences.

https://doi.org/10.1016/j.jrmge.2025.06.019

mechanical heterogeneity induced by the fabrication process, which is an inherent characteristic, has largely been neglected. Consequently, full-scale research is required to assess the applicability of laboratory and simulation results to the engineering scale, providing valuable insights to guide future experimental and numerical investigations.

HLRW research agencies in several countries have conducted studies on full-scale buffer blocks to identify the most effective manufacturing methods. In Sweden, Nuclear Fuel and Waste Management Company (SKB) has conducted systematic research on the preparation of bentonite blocks, examining factors such as raw material property, compaction procedure, and mold geometry (Sanden et al., 2016; Johannesson, 2019). The design diameter of their repository buffer material blocks is 1.65 m. In France, the National Agency for Radioactive Waste Management (ANDRA) used a large-scale press with a force of 60,000 t to produce ring-shaped buffer blocks with a diameter of 2.25 m, a height of 50 cm, a dry density of approximately 1.96 g/cm^3, and a single block weight of about 4 t (Gatabin et al., 2008). In Finland, Posiva Oy conducted block preparation tests using MX80 bentonite, studying the effects of mold type, initial water content, and compaction force on block quality (Holt and Peura, 2011). Finland is the only country currently operating a deep geological repository for HLRW, with the design diameter of its buffer blocks set at 1.7 m (Ville et al., 2020). Due to differences in compaction methods (e.g. rated pressure, pressing direction, mold stiffness, and soil compressibility), different HLRW management agencies have adopted different designs for the size and shape of buffer blocks.

In China, the construction of the Beishan underground laboratory for HLRW disposal commenced in 2021 (Li et al., 2022; Zhao et al., 2023; Zhou et al., 2023). The underground laboratory will conduct 1:1 scale in situ experiments, necessitating the use of large-scale, high-density buffer blocks (Gharbieh et al., 2020; Tan et al., 2021; Wu et al., 2024). To ensure the success of these field tests, it is crucial to investigate the engineering properties of full-scale buffer blocks. Considering batch production efficiency, the current approach of assembling sector-shaped blocks into a ring-shaped buffer barrier is considered a potentially viable option, similar to the scheme adopted by POSIVA (Bosch et al., 2023). Some researchers have prepared fan-shaped blocks to investigate the anisotropy of their swelling pressure and permeability (Tan et al., 2021, 2024; Bosch et al., 2023; Zhu et al., 2024). However, due to the limited capacity of the press, these blocks are typically scaled down by a factor of 3–5 compared to the design dimensions of HLRW repositories, making it difficult to accurately capture the size effect between laboratory and engineering levels.

Besides, the physical and hydro-mechanical heterogeneity of full-scale buffer blocks, caused by stress concentration in corners and stress dissipation from vertical friction, has rarely been reported despite its significant impact on the long-term performance. For instance, non-uniform swelling may lead to internal stress concentrations, accelerating stress relaxation and creep, which weakens the load-bearing capacity over time (Zhao et al., 2019; Zhang et al., 2022). Permeability variations can alter water migration, creating preferential flow paths that reduce the buffer's sealing efficiency (Liu et al., 2020; Xu et al., 2020). Additionally, heterogeneity may induce microcracks, which facilitate water and gas transport, potentially compromising radionuclide containment (Cui et al., 2023). Differences in pore structure further affect ion diffusion and chemical reactions, leading to long-term chemical instability (Ni et al., 2024). Therefore, a comprehensive understanding and precise assessment of buffer block heterogeneity are fundamental to advancing buffer block design.

The primary objective of this study is to experimentally investigate the inherent heterogeneity of full-scale bentonite blocks. A batch of replicated sector-shaped blocks was compacted using a 2000-ton hydraulic press. The physical properties of the blocks, including water content and dry density, as well as their hydro-mechanical properties, such as compressive strength, swelling pressure, and hydraulic conductivity, were selected as key parameters to assess heterogeneity. To analyze the origins of the heterogeneity in clays and moisture, the microstructural characteristics at different positions within the blocks were examined using mercury intrusion porosimetry (MIP) and scanning electron microscopy (SEM). Drawing upon these findings, the feasibility and challenges of estimating the hydro-mechanical properties of blocks from dry density distribution, in conjunction with laboratory-scale results, have been thoroughly analyzed. The outcomes of this study provide valuable theoretical insights for optimizing the buffer design in HLRW repositories and have implications for foundation engineering applications involving axially compressed bentonite.

2. Material and methods

2.1. Raw materials

This study utilized Gaomiaozi (GMZ) bentonite, sourced from Inner Mongolia, China, as the raw materials for buffer blocks. This bentonite has been designated as the preferred buffer material for the Chinese HLRW disposal program (Ye et al., 2015). The bentonite is naturally gray and exhibits a soft texture. To exclude coarse silt and sand particles, the material was refined by sieving through a 74 μm mesh. Fig. 1 shows the particle size distribution curve of GMZ bentonite. Particle size distribution plays a crucial role in soil structure adjustment during compaction. In this study, the GMZ bentonite was processed through grinding and sieving using the same method as in the China Mock-up large-scale test (Liu et al., 2014). The key physicochemical properties of the sieved GMZ bentonite are presented in Table 1 (Zhu et al., 2024).

2.2. Block fabrication

The bentonite is mixed to the desired moisture content to ensure optimal compaction properties. Then, the sector-shaped mold is assembled, and the target mass of bentonite is weighed. The bentonite is then added into the mold in two stages and tamped down to remove any entrapped air. After that, an overhead crane is used to align and close the male and female molds. To

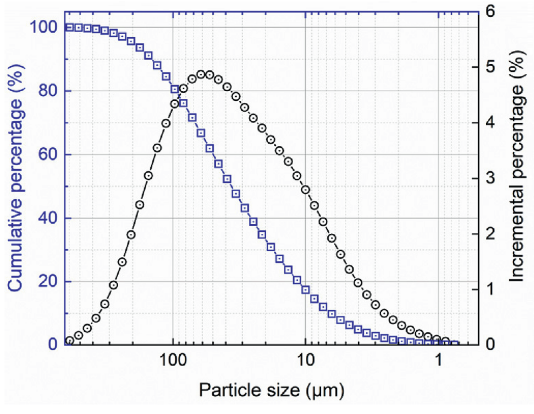

Fig. 1. Particle size distribution curve of GMZ bentonite.

Table 1
Fundamental physicochemical properties of sieved GMZ bentonite.

Parameter	Value
Specific gravity	2.7
Plastic limit (%)	32.8
Liquid limit (%)	208.1
Plasticity index	175.3
Main mineralogical compositions (wt.%)	Montmorillonite (47.7) Quartz (26.3) Feldspar (16.6) Clinoptilolite (7.3) Mica (1.2) Cristobalite (0.9)

ensure safety during the compaction process, a ballistic shield is adopted to enclose both the press and the sector-shaped mold. Once the preparation is complete, the press and control software are activated, with sample parameters inputted, and the compaction method set to single-step control mode. The compaction steps are as follows:

(1) Pre-compaction step. This step uses displacement control with a displacement rate set to 1 mm/min, a target force of 5 kN, and a duration of approximately 10 min. The goal of this step is to ensure sufficient contact between the male mold and the press crossbeam, preventing any tilting of the male mold that could potentially damage the inner surface of the female mold.
(2) Compaction step. After pre-compaction, the displacement target value is set according to the actual compaction height of the sample, with a displacement rate of 5 mm/min (the sample height in this study was 200 mm, with a dry density of 1.9 g/cm^3). During compaction, the pressure head descends to the target height in a single step, i.e. single-step loading. To ensure the reproducibility of the experiments, the specifications of the large-scale press used in this study are listed in Appendix A, Supplementary data Table S1.
(3) Holding step. Once the displacement target value is reached, the displacement is maintained constant for 30 min to allow the sample to stabilize under the applied load. Note that holding time has no significant effect on specimen rebound, as shown in Appendix A, Supplementary data Table S2.
(4) Unloading step. The unloading process is performed at a displacement rate of 1 mm/min, with the target force set to zero.

After compaction, the overhead crane is used to lift the entire sector-shaped mold and move it to an open area. The mold is then disassembled: the male mold is first removed, followed by loosening the bolts in a diagonal pattern. The inner liners of the two female molds are then removed, and finally, the long-arc female mold base is lifted, ensuring that no contact occurs with the compacted block. The sector-shaped blocks have dimensions of an outer diameter of 1200 mm, an inner diameter of 600 mm, and a height of 200 mm, corresponding to an eight-segment division of the ring-shaped buffer block. Critical operations in the fabrication process of full-scale buffer blocks are displayed in Fig. 2.

Since the compacted block is exposed to air and may undergo moisture loss or absorption, it is immediately sealed in plastic film to ensure accurate subsequent measurements of dry density, moisture content, and engineering performance. To maintain the integrity of the block's formation, bentonite with a water content of 13.9 % was used in this experiment, and it is recommended that the water content be maintained between 13 % and 15 % for similar tests (Fig. 3).

2.3. Sample preparation

To investigate the heterogeneity induced by the compaction process rather than the inherent heterogeneity caused by the stacked structure of montmorillonite layers, this study divides the buffer block into different regions to compare variations in physical and hydro-mechanical properties. As shown in Fig. 4a, the buffer block was divided into 9 regions along the horizontal cross-section, labeled A1 to A9. Core samples were extracted from different regions using an SC-200 automatic rock coring machine. For the physical property tests, each bentonite core was then segmented into 8 equal segments along the compacting direction, labeled Layer 1 to Layer 8. For the hydro-mechanical property tests, the core sampling positions are shown in Fig. 4c. The bentonite cores were divided into three sections, labeled 1 to 3 (Fig. 4d). In the axial direction, Section 1 was at the top and Section 3 at the bottom, while in the radial direction, Section 1 was at the inner edge and Section 3 at the outer edge.

2.4. Test methods

2.4.1. Unconfined compression

The experiments were conducted using a WDW-20 microcomputer-controlled electro-hydraulic servo testing machine to perform unconfined uniaxial compression tests on the prepared samples. The stress-strain relationship was recorded during the test.

2.4.2. Swelling pressure

The circular disc-shaped sample was placed into the constant-volume cell with permeable stone on both surfaces. A preloading pressure of 0.1 MPa was applied to eliminate gaps between components. It was submerged in a water bath with deionized water. During the test, the bentonite swelled under its own suction, with swelling pressure recorded by a force sensor. The test ended when the swelling pressure changed by less than 1 % over 24 h. To minimize the impact on the sample's dry density and water content, the cored samples were not subjected to surface grinding or polishing.

2.4.3. Permeability characteristics

After the swelling pressure test, a water pressure of 10–50 kPa was applied to the disc-shaped sample using a constant pressure/volume controller (CPV controller). Then the water pressure was increased to 1000 kPa and maintained throughout the test. Inlet pressure and flow rate were continuously recorded. The test ended once stable outflow was observed (infiltration volume equals the exfiltration volume), indicating the sample was fully saturated. The hydraulic conductivity k (m/s) is calculated as follows:

$$k = \frac{Q}{A\Delta h} \tag{1}$$

where Q (m^3/s) is the flow rate, A (m^2) is the cross-sectional area, and Δh (m) is the head difference.

2.4.4. Microstructure features

Mercury Intrusion Porosimetry (MIP) was conducted to examine the pore structure of the clay samples. Cubic samples, with side lengths ranging from 0.4 cm to 1 cm, were extracted from the blocks for analysis. The MIP measurements were performed using an AutoPore IV 9500 instrument (Micromeritics, USA). In addition, SEM was employed to investigate microcracking within the blocks, utilizing a Gemini 300 device (Carl Zeiss, Germany). Prior to these microstructural tests, all samples underwent freeze-drying.

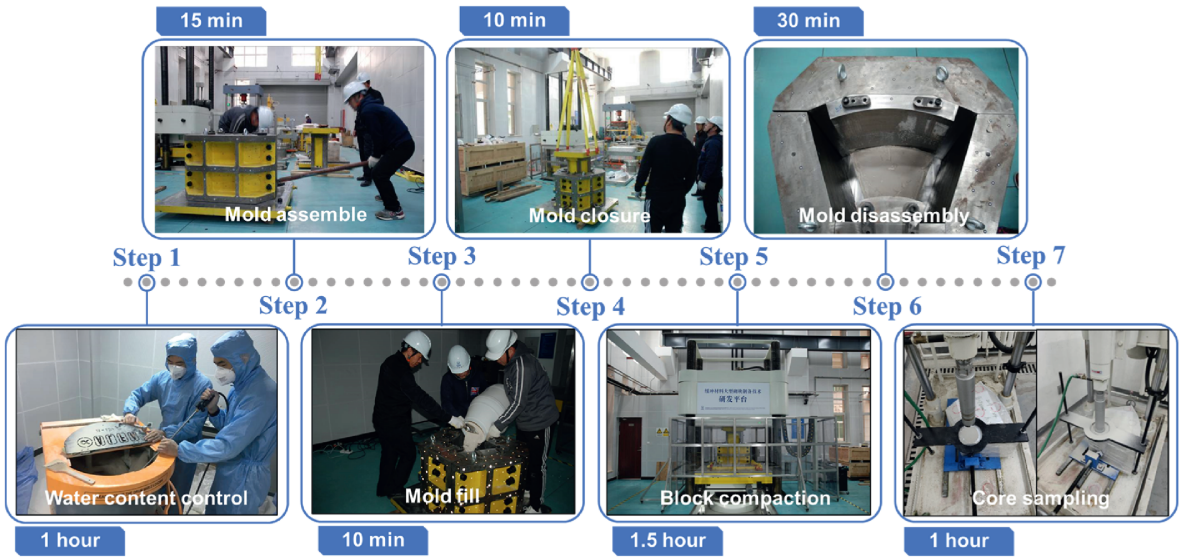

Fig. 2. Critical operations in the fabrication process of full-scale buffer blocks (The time indicated in the blue boxes corresponds to the duration required for each step).

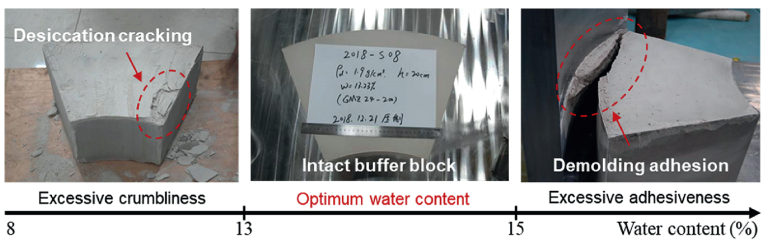

Fig. 3. Comparison of the moldability of bentonite with different initial water contents.

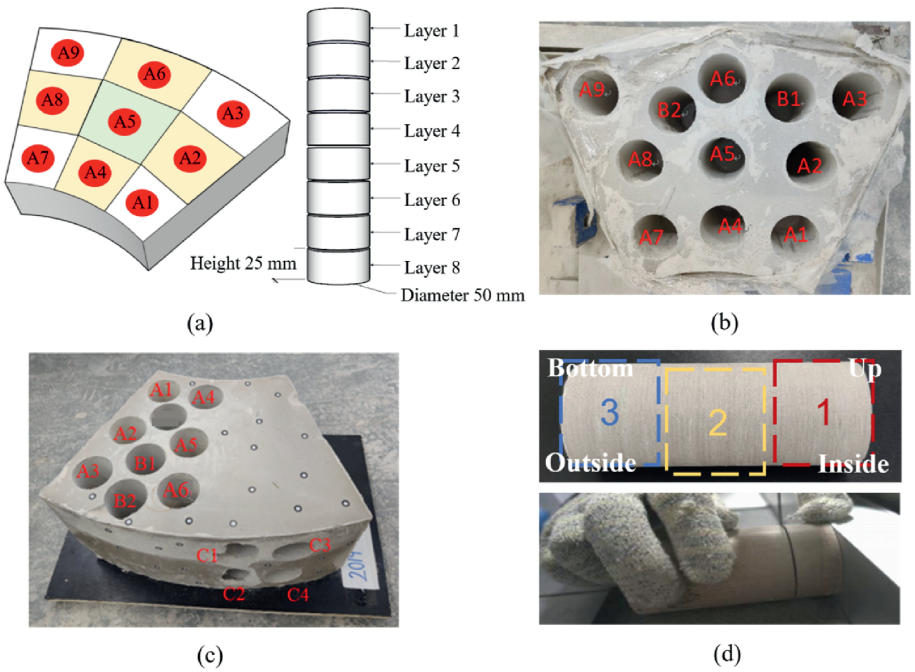

Fig. 4. Core sampling of sector-shaped blocks: (a) Sampling positions for physical heterogeneity testing; (b) Core-drilled blocks used for physical heterogeneity testing; (c) Core-drilled blocks used for hydro-mechanical behavior testing; and (d) Clay core segmentation for hydro-mechanical behavior testing.

3. Results

3.1. Distribution characteristics of physical properties

3.1.1. Soil water distributions

Fig. 5 presents the water content distribution within a compacted bentonite block at 8 different depths, labeled as Layers 1 to 8 in subfigures (a) to (h), respectively. Each layer corresponds to an evenly segmented horizontal section of the bentonite block along the compacting direction. The water content is visualized using contour maps, with values ranging from approximately 13.52 %–14.14 %, as indicated by the accompanying color scale. The *X* and *Y* axes represent the relative axial and radial positions within each horizontal section, facilitating a spatial analysis of water content variability as illustrated in Fig. 5i.

In the shallow layers (Layers 1 and 2), the water content exhibits a clear gradient, with higher values on the left side and lower values on the right. The left corner regions show a noticeable concentration of moisture, exceeding 13.84 %. In Layers 3 and 4, the moisture concentration begins to shift to the bottom-right corner, reaching 13.92 %. The radial gradient becomes less pronounced, indicating a more symmetrically distributed moisture profile compared to the upper layers. In Layers 5 and 6, the moisture content is higher along the sides and lower in the center. This pattern is accompanied by an increase in the heterogeneity of moisture distribution, especially in the central areas, where moisture levels decrease significantly. This suggests that moisture is preferentially accumulating along the edges, creating a more uneven distribution. By Layer 7, the moisture distribution stabilizes, shifting from the previous side-high, center-low pattern to a more uniform distribution, indicating a migration of moisture from the edges toward the center. Finally, in Layer 8, the deepest section, a prominent high-moisture zone (14.07 %) forms near the center of the block. This zone is surrounded by regions with slightly lower water content (13.65 %), marking the establishment of a centralized moisture accumulation in the deepest layers.

Fig. 6 presents the moisture distribution across three vertical sections, labeled A1-A3, A4-A6, and A7-A9, from right to left.

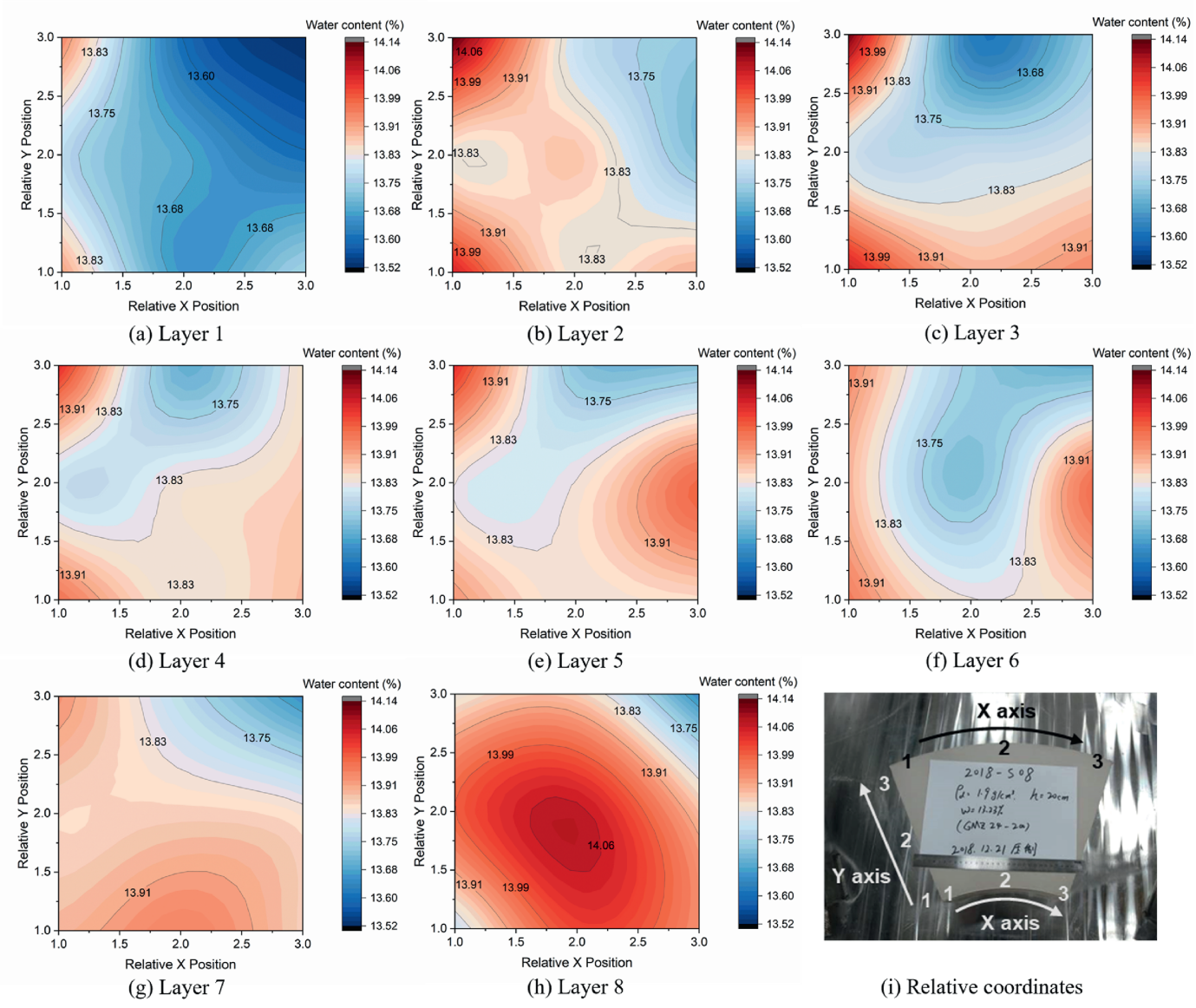

Fig. 5. Water content at different heights of the buffer block ($y = 1$ corresponding to the short edge, $y = 3$ corresponding to the long edge).

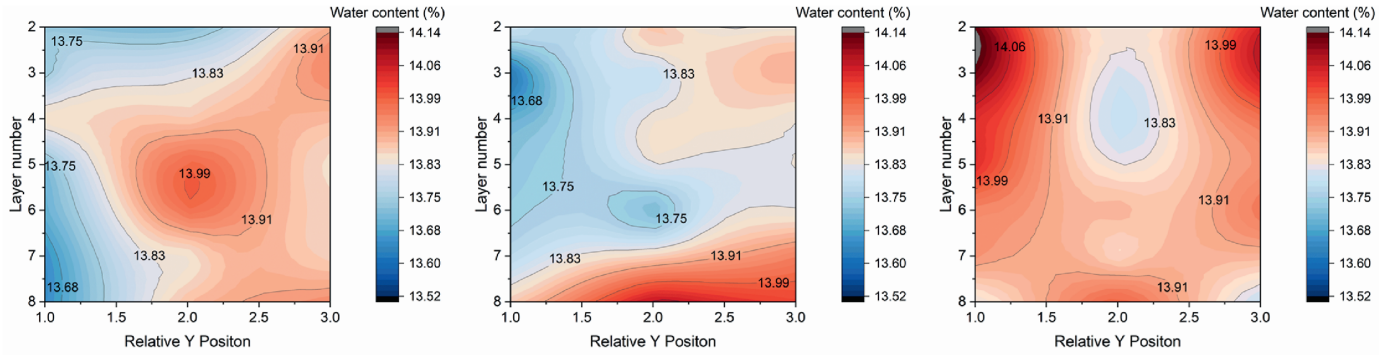

Fig. 6. Water content at different vertical cross-sections of the buffer block ($y = 1$ corresponding to the short edge, $y = 3$ corresponding to the long edge).

Section A1-A3 displays a central concentration of moisture, with reduced moisture values in the corner regions along the long edges of the fan-shaped section. Section A4-A6 shows a progressive increase in water content both vertically (from top to bottom) and horizontally (from left to right), with the peak moisture concentration located at the center of the bottom layer. In Sections A7-A9, a symmetric moisture distribution is observed, characterized by lower moisture at the center and higher values at the sides. A localized moisture concentration is evident in the corner region on the left side of the block, which diminishes with increasing depth. In general, vertical moisture transport in the central section is more uniform and continuous, while the lateral sections display a contrasting distribution pattern.

Overall, the moisture variation within the block is limited to 4.6 %. In the horizontal plane, moisture variation ranges from 2 % to 3.7 %, while along the longitudinal section, it spans from 2.3 % to 3.5 %. These results suggest that moisture transport efficiency is similar in both horizontal and vertical directions, implying that the compaction process has not formed a preferential flow path in any single direction.

3.1.2. Variations in compaction degree

The dry density distribution across various horizontal sections is presented in Fig. 7, with values ranging from approximately 1.76 g/cm^3 to 1.86 g/cm^3. The rebound after unloading resulted in the actual dry density being slightly lower than the target value (Chen et al., 2017). Layer 1, the shallowest layer, exhibits a clear centrosymmetric distribution, characterized by lower density values at the center (1.82 g/cm^3) and progressively higher values toward the periphery (1.85 g/cm^3). This pattern suggests a uniform compaction process at the surface level. As the depth increases, however, Layers 2 to 4 no longer maintain this centrosymmetric distribution. The localized variations in compaction are particularly evident in the corner regions, where vertical friction plays a significant role in the redistribution of stress. Despite these shifts, the general trend of lower density at the center persists, which can be attributed to the inherent nature of stress dissipation within the granular material. In Layer 5, a notable change occurs: three corner regions (excluding the top-right) transition into low-density zones (about 1.81 g/cm^3), while the central area becomes the high-density region (1.84 g/cm^3). Interestingly, the depth at which this reversal in dry density distribution occurs is shallower than that observed for the water content, indicating a delayed response in liquid transport relative to solid compaction under the influence of vertical stress. In Layers 6 to 8, the dry density distribution gradually reverts to a centrosymmetric pattern, completing the reversal process initiated in Layer 5 (lower density at the corner region decreases to 1.76–1.78 g/cm^3). Additionally, the high-density region (1.8–1.84 g/cm^3) at the center expands as the depth increases, reflecting the ongoing effects of compaction and stress redistribution at greater depths.

The dry density distribution across different vertical sections is shown in Fig. 8. Different from the water content distribution, the dry density in the A1-A3 and A7-A9 sections exhibits a strong similarity, with both showing a decreasing trend in dry density as depth increases. Notably, the A4-A6 section features a low-density region in the middle-upper region, which is likely the result of uneven accumulation of granular material during the stacking process. Despite this, the overall trend in this section also shows a reduction in dry density with increasing depth. Besides, the dry density in the A4-A6 section ranges from 1.81 g/cm^3 to 1.85 g/cm^3, which is slightly narrower than the ranges observed in the A1-A3 and A7-A9 sections, where dry density values span from 1.78 g/cm^3 to 1.86 g/cm^3 and 1.76 g/cm^3 to 1.85 g/cm^3, respectively. This variation emphasizes the impact of vertical friction-induced stress dissipation on the heterogeneity in dry density.

In general, the fluctuation range of dry density is within 5.6 %, with greater variations observed in the vertical plane (2.2 %–4.6 %) compared to the horizontal plane (2.3 %–2.8 %). Moreover, only the horizontal sections along the vertical direction exhibit a transition to opposing distribution patterns, indicating a more significant reconfiguration of the dry density profile with increasing depth. These results suggest that solid transport predominantly occurs in the vertical direction.

3.2. Hydro-mechanical properties of full-scale block

3.2.1. Mechanical property

Fig. 9a shows the compressive strength and elastic modulus of clay cores taken from different positions. Since the mechanical tests were conducted on 50 mm × 100 mm samples (diameter × height), only one sample could be tested per core due to material loss during the coring and polishing process. In this study, mechanical testing was performed on clay samples from the upper, middle, and radial sections of the block. The results indicate that the compressive strength and elastic modulus of the clay samples exhibit similar trends. The mechanical strength of the tested samples ranged from 5.8 MPa to 7.6 MPa, while the elastic modulus varied between 225 MPa and 314 MPa, demonstrating significant heterogeneity. Given the limited sample size, the variation in the block's maximum mechanical parameters could be even more pronounced. Clay samples from the upper corner region exhibited the highest mechanical properties, with a rapid decrease in strength as the sampling location moved towards the central

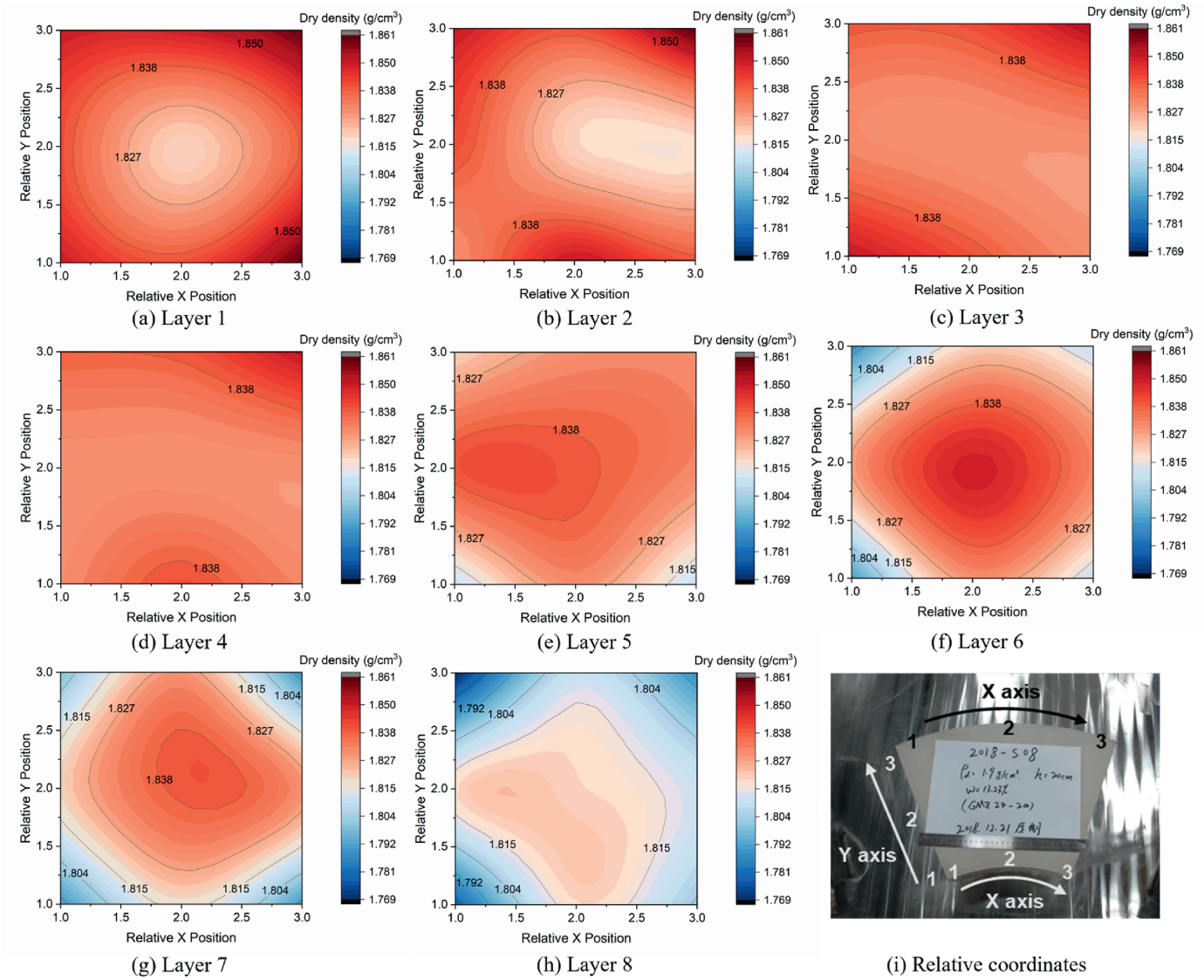

Fig. 7. Dry density at different heights of the buffer block ($y = 1$ corresponding to the short edge, $y = 3$ corresponding to the long edge).

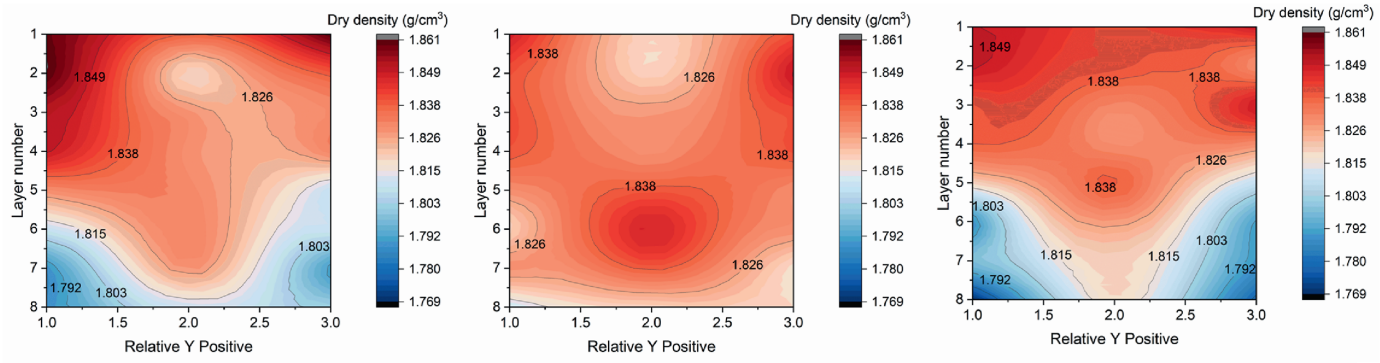

Fig. 8. Dry density at different vertical cross-sections of the buffer block ($y = 1$ corresponding to the short edge, $y = 3$ corresponding to the long edge).

areas of the block. Overall, a trend emerged where the mechanical properties became more stable towards the core of the block. Additionally, clay cores taken radially displayed significantly weaker mechanical properties compared to axially sampled cores from similar horizontal layers, suggesting the potential formation of directional plastic damage within the block during the compaction process.

Clay samples were taken near the coring locations, and the dry

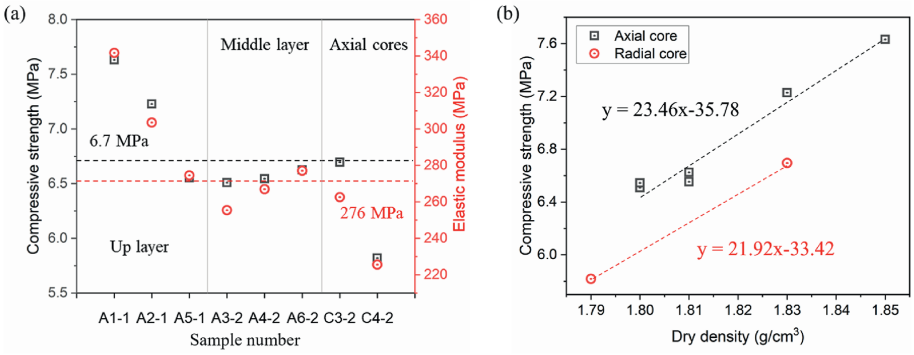

Fig. 9. Mechanical parameters at different locations within full-size blocks: (a) Compressive strength and elastic modulus; and (b) Relation of compressive strength and dry density.

density of the samples was calibrated using the wax-sealing method (Fan et al., 2010). The results revealed a strong linear correlation between the mechanical strength of the cores and their dry density, as shown in Fig. 9b. As the dry density increased, the compressive strength of both axial and radial soil cores exhibited similar growth rates. This suggests that the mechanical anisotropy of the block and its distinct regions may be characterized by a specific anisotropy constant, which requires further systematic mechanical testing for a more detailed investigation.

3.2.2. Swelling pressure

Swelling pressure tests were performed on a batch of clay cores sampled from different positions within the block, with the corresponding dry density and swelling pressure data presented in Appendix A, Supplementary data Table S3. The swelling pressure of the clay cores from sample S1 ranged from 1.9 MPa to 4.7 MPa, while that of the cores from sample S2 ranged from 2.7 MPa to 6.1 MPa, exhibiting considerable variability. Fig. 10 illustrates the relationship between dry density and swelling pressure. Due to the inevitable unevenness on the side surfaces of the cores caused by drilling, although the clay samples were polished, the surfaces of the cores did not perfectly conform to the confinement walls. As a result, the swelling pressure data exhibit some degree of dispersion. Nevertheless, a good positive linear correlation between swelling pressure and dry density is evident, with a Pearson correlation coefficient of 0.698, which is consistent with both the experimental results from compacted specimens and the simulation outcomes (Tanaka and Watanabe, 2019; Han et al., 2021; Wang et al., 2022). The Pearson correlation coefficient can be calculated as Eq. (2). This indicates that, despite the plastic deformation and potential microcracking caused by variations in compaction degree and stress distribution during the compaction process of full-scale blocks, dry density remains the primary factor influencing swelling pressure. Therefore, it is feasible to estimate the swelling pressure distribution using dry density distribution data. Due to the experimental system errors mentioned above, the difference between radial and axial swelling pressures could not be determined. Further research is needed to investigate the anisotropy of swelling pressure in a full-scale block, potentially by using less abrasive coring methods or a flexible confinement system.

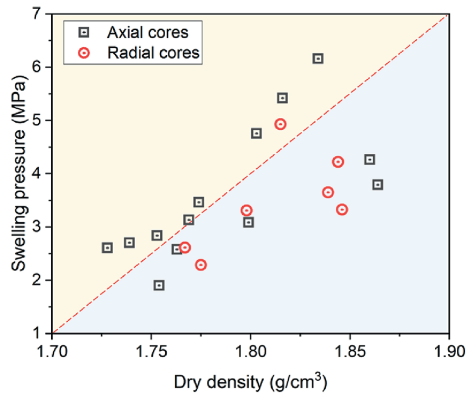

Fig. 10. Relation of maximum swelling pressure and dry density within full-scale blocks.

$$r = \frac{\sum (X_i - \overline{X})(Y_i - \overline{Y})}{\sqrt{\sum (X_i - \overline{X})^2 \sum (Y_i - \overline{Y})^2}} \quad (2)$$

where X_i and Y_i are the individual data points in the two variables X and Y, respectively; $\overline{X}$ and $\overline{Y}$ are the means of the variables X and Y, respectively.

3.2.3. Hydraulic conductivity

After measuring the swelling pressure, the samples were subjected to permeability testing without removing the molds. The measured hydraulic conductivities are presented in Table S3. The results show that the hydraulic conductivity of the clay cores from sample S1 ranged from 3.29×10^{-13} to 9.23×10^{-13} m/s, while that of the clay cores from sample S2 ranged from 9.77×10^{-14} to 5.33×10^{-13} m/s. Notably, the variation in hydraulic conductivity (2.8 times for S1, 5.4 times for S2) was significantly greater than that of the swelling pressure (2.4 times for S1, 2.2 times for S2). As shown in Fig. 11, the hydraulic conductivity of the clay cores generally decreases with increasing dry density, and the difference between the axial and radial hydraulic conductivities cannot be determined from the data. The permeability coefficient exhibits a strong negative linear correlation with dry density, with a Pearson correlation coefficient of −0.841. When the dry density exceeds 1.7 g/cm^3, the hydraulic conductivities of all the clay cores meet the design requirement (less than 1×10^{-12} m/s). Therefore, in determining the design parameters for the block, it is crucial to account for the risk of locally low hydraulic conductivities resulting from dry density heterogeneity.

3.3. Microstructural observations

3.3.1. Pore structure characteristics

The pores in compacted bentonite are typically categorized into three types: interlayer pores, interparticle pores (intra-aggregate

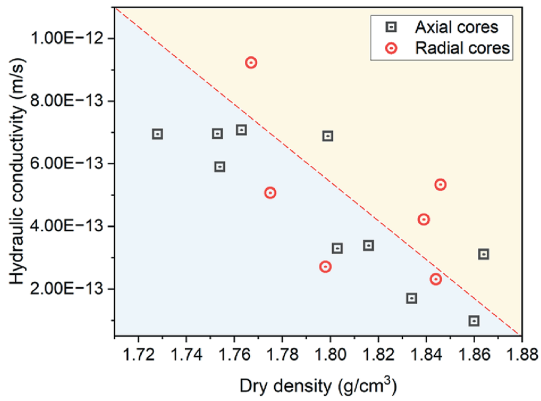

Fig. 11. Relation of hydraulic conductivity and dry density within full-scale blocks.

pores), and inter-aggregate pores (Delage, 2010). Fig. 12 illustrates the pore structure characteristics at different depths in the corner, edge, and center regions of the block, as obtained through MIP.

As shown in the upper row of Fig. 12, the cumulative mercury intrusion curve reveals significant variability in the total pore volume in the corner and edge regions of the block, with an increasing trend in pore volume with depth. In contrast, the total pore volume at the center of the horizontal cross-section shows greater stability. This is consistent with the dry density test results (Figs. 7 and 8). It is important to note that due to the resolution limitations of the technique, with a minimum detectable pore size of approximately 5 nm, interlayer pores (ranging from 0.2 nm to 2 nm) are undetectable, leading to a slight underestimation of the actual porosity. As shown in the bottom row of Fig. 12, the pore distribution generally exhibits a bimodal pattern, enabling the classification of detected pores into two categories: inter-aggregate pores (macro-pores) and interparticle pores (micro-pores). The pore diameter boundary used to differentiate between these types is set at 150 nm, which aligns with the value determined using the 'valley' criterion (Ye et al., 2010). At different depths, the micro-pore volume in the corner and edge regions remains relatively constant, while the variations in total porosity are primarily governed by the compressive deformation of the macro-pores. Especially, in the upper layers of the corner and edge regions, the peak associated with the macro-pores nearly vanishes, indicating that the bentonite in these regions has achieved its maximum compaction. In general, the pore structure heterogeneity follows the order: corner regions > edge regions > center regions, and upper layer > middle layer > lower layer.

3.3.2. *Microstructural morphology*

As shown in Fig. 13, the microstructural morphology of the clay samples at different positions is presented, with the average dry density of each region marked in the subfigures. Microcracks of varying degrees were observed in all nine SEM images, with the cracks primarily oriented along the axial direction (compaction direction), indicating localized tensile damage resulting from uneven stress distribution during the compaction process (Zhang et al., 2022). This suggests that the anisotropy of the hydro-mechanical properties of the compacted bentonite in the block could be further exacerbated by the presence of longitudinal microcracks (e.g. as shown in Fig. 9). Although MIP results indicate that the corner and edge regions of the upper layer have reached maximum compaction, SEM images reveal the existence of microcracks, suggesting that these cracks likely formed during the unloading or settling process.

Microcrack development seems to be more closely linked to the relative dry density within the same horizontal layer than to the absolute dry density. For instance, the corner region in the upper layer and the center region in the middle layer, both with the

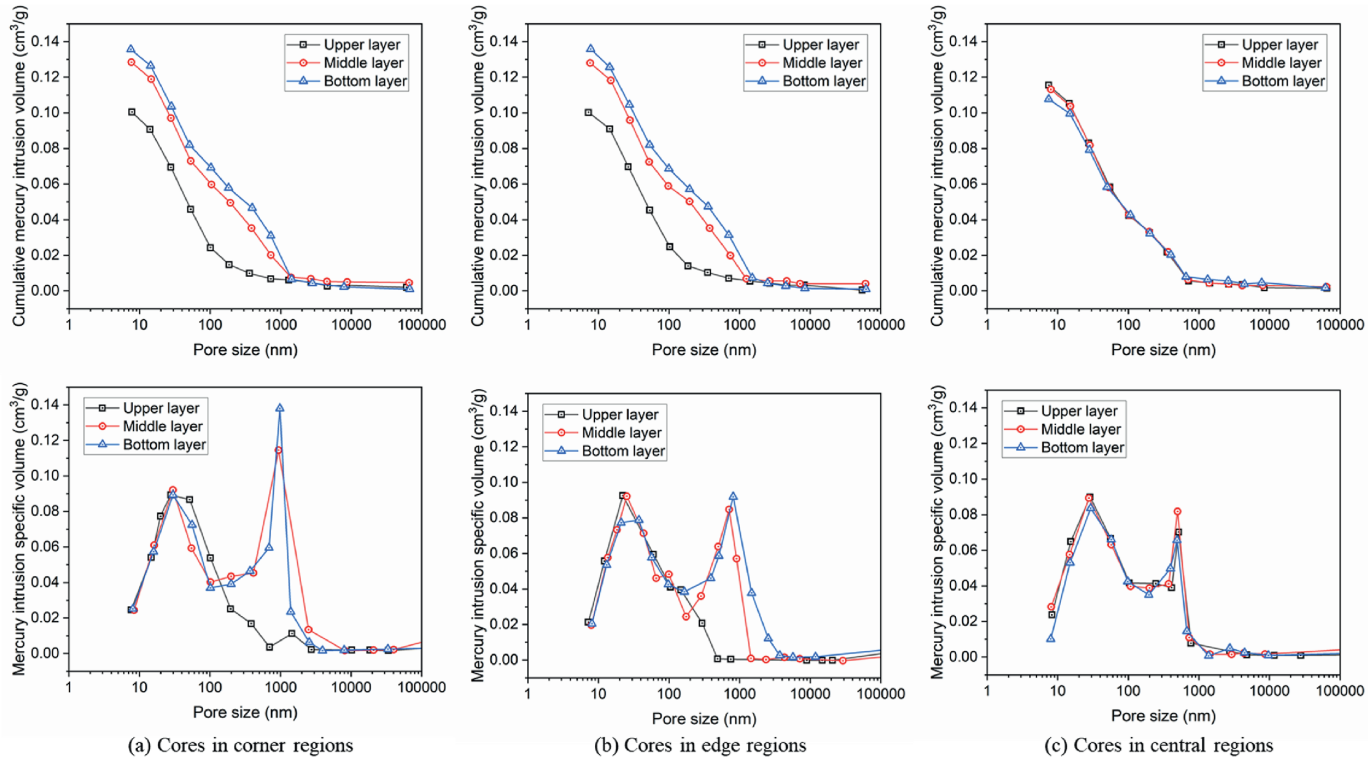

Fig. 12. Pore structure characteristics at different positions within the full-scale block.

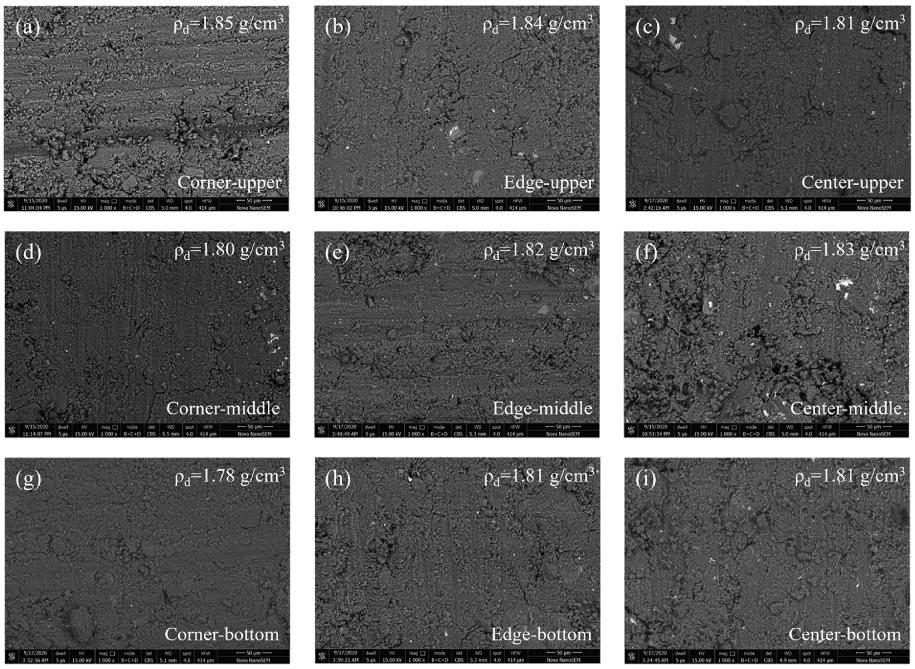

Fig. 13. Morphology observations of compacted bentonite at different positions within the full-scale block (1000× magnification).

highest dry density, show the most pronounced microcracks. In contrast, the lower layer, with generally lower dry density, exhibits fewer microcracks. During unloading, the stress distribution within the block becomes more uniform as the unloading pressure approaches zero (Wang et al., 2023). Regions with higher dry density unload more rapidly, making them more susceptible to plastic deformation. At the same time, vertical rebound occurs, while horizontal constraints remain, resulting in longitudinal cracks due to horizontal tensile stresses (Tanaka et al., 2014; Tong et al., 2024). It is noteworthy that microcracks in regions with higher dry density make it more difficult to achieve higher compaction, with the relationship between target dry density and required maximum pressure often being exponential (Tanaka and Watanabe, 2019; Han et al., 2021; Wang et al., 2022).

4. Discussion

4.1. Origins of the heterogeneity in soil-moisture distribution

The results from the soil-moisture distribution tests indicate that, in the upper layer, water content and dry density follow distinct distribution patterns. However, with increasing depth, their distributions converge, and the lower layer exhibits a centrosymmetric pattern, with higher values at the center and lower values at the edges. This suggests a strong correlation between water content and dry density in the middle and lower layers (e.g. as shown in Fig. 14a). As shown in Fig. 14b and c, the water content range (13.52 %–14.14 %) in the blocks corresponds to a stable (or metastable) 2-layer state in the montmorillonite crystal structure, regardless of the wetting or drying path (Sun et al., 2014; Dai et al., 2025). Thus, the uneven water content distribution does not induce differential swelling behaviors in the montmorillonite. Furthermore, as illustrated in Fig. 14d, moderate water content enhances the compressibility of bentonite. However, when the water content exceeds 15 % or when the dry density approaches approximately 1.85 g/cm^3, the impact on compressibility becomes negligible. Consequently, water content primarily affects dry density by altering the elastoplastic deformation of macro-pores, rather than influencing micro-pores and interlayer pores, which is consistent with the MIP results (Wang et al., 2013; Qiao et al., 2019).

Based on the analysis of MIP and SEM results, it is evident that the upper layer of the block is approaching its maximum dry density. During the compaction process, the expulsion of gases from the bentonite predominantly occurs along the mold's sidewalls, resulting in lower compaction at the center due to the longer path for gas expulsion (Davy et al., 2009; Cui et al., 2022). Furthermore, in the upper layer of the block, some moisture migrates downward, while a portion is expelled laterally. Given that the male and female molds fit least effectively in the corner regions, moisture tends to preferentially migrate toward these areas. With increasing depth, the dissipation of compaction stress through lateral friction gradually results in a good correlation between the dry density and water content distributions. In the presence of overlying bentonite layers (which limit lateral moisture expulsion), the downward infiltration of moisture through vertical microcracks increases, primarily migrating from regions of lower dry density toward the lower layers (Liu et al., 2021). As a result, the heterogeneity in the upper layer amplifies that in the lower layer. A comparison of Figs. 5 and 7 reveals that in the middle layer, the bentonite underlying areas with lower dry density tends to accumulate moisture, thus supporting this inference. Additionally, considering that the water content in the blocks in this study ranges from 13.52 % to 14.14 %, the increase in water content promotes further compaction of the bentonite. As a result, the dry density in moisture accumulation zones of the bottom layer gradually increases, with low-density areas transitioning to higher-density regions. As both moisture and compaction levels adjust, a trend toward homogenization of water content and dry density is observed across the horizontal cross-section with increasing depth. Overall, the heterogeneity of the blocks primarily arises from differences in expulsion paths of water and gas during compaction, leading to uneven moisture migration and altered soil compressibility. Additionally, side friction further exacerbates this heterogeneity.

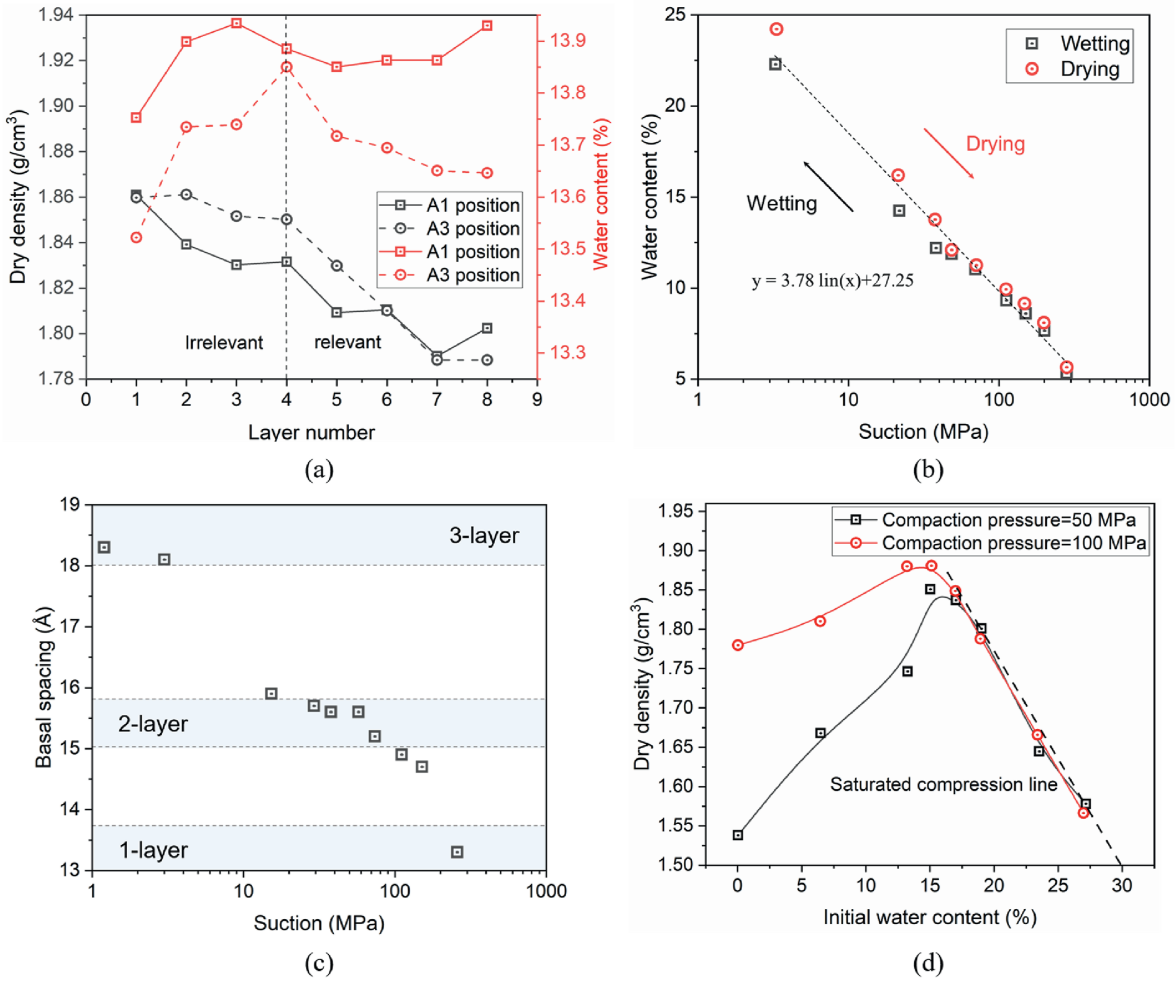

Fig. 14. Correlation analysis of dry density and water content distribution in the block: (a) Evolution of dry density and water content in the corner region; (b) Soil water retention curves; (c) Crystalline swelling curve; and (d) Compaction curves.

4.2. Estimation of the hydro-mechanical properties of full-scale block

Mechanical strength, swelling pressure, and hydraulic conductivity are key parameters for evaluating block quality and predicting the long-term evolution of buffer layer properties (Liu, 2013; Joseph et al., 2017; Li et al., 2022). This study reveals that the hydro-mechanical properties at different positions within the block are strongly correlated with dry density, suggesting that the heterogeneity of hydro-mechanical properties can be inferred from dry density distribution in conjunction with laboratory-scale results. Since dry density testing requires minimal clay sample volume and is relatively straightforward, it significantly reduces the difficulty of obtaining hydro-mechanical property data and enhances data resolution.

For example, numerous laboratory-scale studies have established an exponential relationship between dry density and swelling pressure. Wang et al. (2022) established that the relationship between dry density and maximum swelling pressure for compacted bentonite at varying initial water contents can be described by Eq. (3).

$$p_s = 5.13 \times 10^{-4} \rho_d e^{5.26} \tag{3}$$

where p_s is the maximum swelling pressure, ρ_d is the initial dry density, and e is the natural constant.

By using Eq. (3), the dry density distribution can be converted into a swelling pressure distribution map, as shown in Fig. 15. The results reveal that the variation of swelling pressure within the block ranges from 5.15 MPa to 8.4 MPa, with an amplitude of 63.1 %, significantly higher than the fluctuations in dry density and water content. This indicates that the uneven distribution of swelling pressure in the block may pose a shear failure risk to both the waste container and the overlying backfill layer (Sample-Lord et al., 2021; Pintado et al., 2023). Additionally, bentonite blocks are affected by the decay heat of HLRW, which increases the temperature and promotes the crystalline swelling of montmorillonite, further exacerbating the uneven distribution of swelling pressure within the blocks (Stephanie et al., 2015; Yang et al., 2021). Therefore, in finite element simulations, it is essential to account for the variation in initial parameters at different positions, which is crucial for accurately modeling the long-term performance of the buffer layer.

Notably, predicting the hydraulic heterogeneity of the block based on laboratory-scale results has certain limitations. Firstly, the anisotropy of hydraulic properties at different positions within the block is challenging to infer from laboratory-scale experiments. The moisture migration and stress distribution within the block during compaction are more complex than those observed at the laboratory scale. Direct determination of the material's

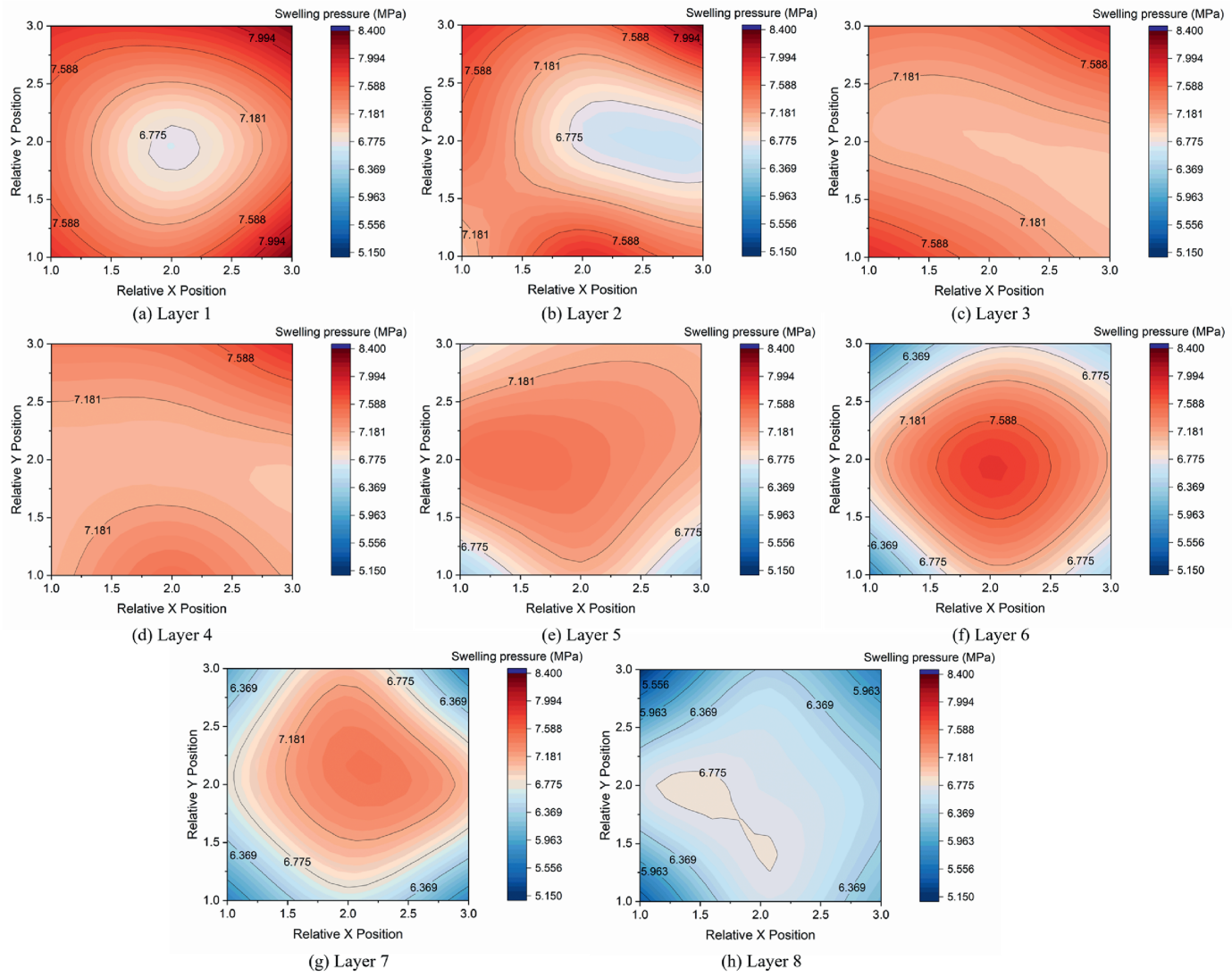

Fig. 15. Swelling pressure at different heights of the buffer block ($y = 1$ corresponding to the short edge, $y = 3$ corresponding to the long edge).

anisotropy coefficients using characterization techniques will offer valuable theoretical support for predicting the block's overall and local anisotropy (Peng et al., 2022). For instance, Dai et al. (2025) found via X-ray diffraction (XRD) texture analysis that compaction enhances bentonite particle alignment. Compression brings charged particles closer, inducing a double-layer effect that promotes face-to-face arrangement. Macroscopically, this leads to the preferential orientation of montmorillonite (001) planes along the compaction direction, significantly influencing its hydro-mechanical behavior (Zhang et al., 2012; Lu et al., 2023; Zhu et al., 2024). Secondly, vertical microcracks (similar to micro-joints in rock) form to varying extents at different locations within the block, further contributing to its anisotropy. While these microcracks can be observed using μ-CT, quantifying them remains challenging (Diaz et al., 2023). Thus, the development of vertical microcracks in the block requires further investigation. Moreover, studying the anisotropy of full-scale blocks through experimental methods is time-consuming and labor-intensive. Simulating the compaction process of sector-shaped blocks with varying dimensions, dry densities, and initial water contents would significantly reduce the cost of similar studies.

4.3. Assessment of the global heterogeneity of buffer blocks

Given the strong correlation between dry density and hydro-mechanical properties, dry density is chosen to characterize the heterogeneity of buffer blocks. The heterogeneity for a specific section can be assessed as follows:

$$H_i' = \left| \frac{\rho_{di} - \overline{\rho_d}}{\overline{\rho_d}} \right| \tag{4}$$

$$H' = \frac{\sum H_i'}{k} \tag{5}$$

where H_i' represents the heterogeneity coefficient at different test points, $\overline{\rho_d}$ is the average dry density of that section, H' is the heterogeneity coefficient for a specific section, and k is the number of test points in a given section.

Considering the orientation preference of clay particles induced by uniaxial compaction, anisotropy should be comprehensively accounted for in determining the global heterogeneity coefficient of buffer blocks. However, the heterogeneity observed in a single cross-section may not accurately represent the heterogeneity

Table 2
Global heterogeneity coefficients and hydro-mechanical properties of buffer blocks.

Sample number	Target dry density (g/cm^3)	Global heterogeneity coefficient	Swelling pressure fluctuation rate	Hydraulic conductivity fluctuation rate
S1	1.8	0.006204	−35.9 % to 30.5 %	−48.7 % to 43.7 %
S2	1.9	0.011024	−33.7 % to 50.8 %	−67.1 % to 79.4 %

along a particular direction. To minimize potential variability in the experimental results, this study uses the heterogeneity from a set of parallel cross-sections to characterize the directional heterogeneity. The global heterogeneity coefficient H can be determined using Eq. (6):

$$H = \alpha H_a + \beta H_r \tag{6}$$

where α and β are the weighting coefficients for axial and radial directions, respectively. H_a and H_r are the heterogeneity coefficients for axial and radial direction, respectively, which can be determined as follows:

$$H_a = \sum \lambda_i H_{ai}' \tag{7}$$

$$H_r = \sum \gamma_j H_{rj}' \tag{8}$$

where λ_i and γ_j are the impact coefficients of sections i and j on the global heterogeneity, respectively. H_{ai}' and H_{rj}' are heterogeneity coefficients for axial and radial directions, respectively.

Based on the results of mechanical properties, the impact of physical heterogeneity is greater in the axial direction than in the radial direction, which cannot be accurately captured by dry density. Therefore, suitable indicators for describing the anisotropy of compacted bentonite are required to determine the values of α and β. According to the work of Dai et al. (2025), the orientation index (OI) of compacted bentonite can be determined from the XRD pattern as follows:

$$OI = \frac{I_{001}}{I_{060}} \tag{9}$$

where I_{001} and I_{060} are the intensity of (001) and (060) reflections, respectively.

Notably, under the same relative humidity (RH) conditions, the orientation index shows a positive correlation with dry density (Dai et al., 2025). Therefore, the values of α and β can be determined using the following equations:

$$\alpha = \frac{OI_{\rho_{target}}}{1 + OI_{\rho_{target}}} \tag{10}$$

$$\beta = \frac{1}{1 + OI_{\rho_{target}}} \tag{11}$$

where $OI_{\rho_{target}}$ is the orientation index for the target dry density.

In the meanwhile, impact coefficients λ_i and γ_j are associated with the origins of the heterogeneity in soil-moisture distribution. As for λ_i, its value gradually decreases with depth since the heterogeneity of the upper layer affects the lower layer during uniaxial compression, while the lower layer has no impact on the upper layer. As for γ_j, its value remains constant as there is no significant interaction between the heterogeneity of different radial sections. Therefore, the value of λ_i and γ_j can be tentatively calculated as follows:

$$\lambda_i = \frac{n - i}{\sum_{k=1}^{n-1} k} \tag{12}$$

$$\gamma_j = \frac{1}{m} \tag{13}$$

where i represents the section number counted from top to bottom, n denotes the total number of axial sections, and m refers to the total number of radial sections.

Overall, a smaller global heterogeneity coefficient H indicates lower heterogeneity in the buffer block. Table 2 presents the global heterogeneity coefficient, swelling pressure fluctuation rate, and hydraulic conductivity fluctuation rate for blocks S1 and S2 (detailed data in Table S3). The results show that the global heterogeneity coefficient of the block with a target dry density of 1.9 g/cm^3 is 77.3 % higher than that of the block with a target dry density of 1.8 g/cm^3, consistent with the variations in swelling pressure and hydraulic conductivity fluctuation rates. This finding preliminarily suggests that the global heterogeneity coefficient

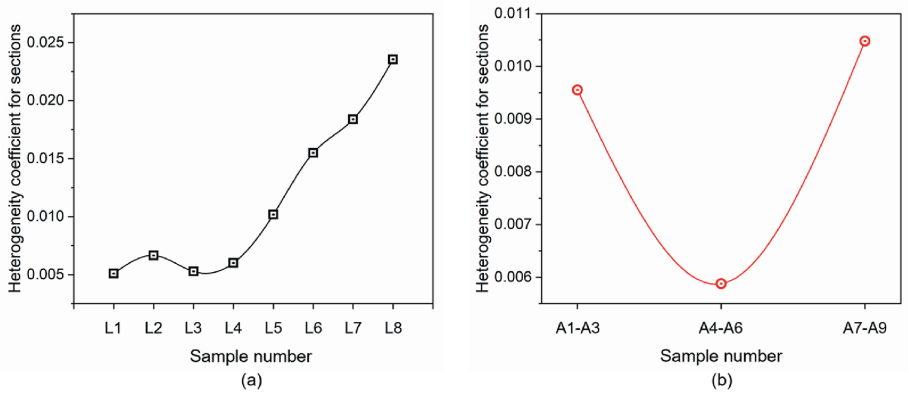

Fig. 16. Heterogeneity coefficients of sections for buffer block: (a) Horizontal section; and (b) Vertical sections.

provides good resolution for assessing fluctuations in hydro-mechanical properties.

This approach not only assesses the overall heterogeneity of the blocks but also quantitatively analyzes heterogeneity at different sections. By substituting the data from Figs. 6 and 7 into Eqs. (4)–(8), the axial and circumferential heterogeneity distribution of the block can be determined. As shown in Fig. 16a, the heterogeneity coefficient exhibits an exponential relationship with depth, characterized by lower heterogeneity in the upper layer, a significant increase in the middle layer, and a further acceleration in the lower layer. This underscores the cumulative nature of heterogeneity during compaction, where heterogeneity in the upper layer exacerbates that of the lower layers. Furthermore, it highlights two key strategies for improving the axial homogeneity of the block: controlling the heterogeneity in the upper layer and mitigating its accumulation along the depth direction. Therefore, pre-compaction to enhance the contact between the punch and the bentonite surface, along with multi-layer compaction, are potential methods for improving axial homogeneity. As shown in Fig. 16b, the heterogeneity coefficient is significantly higher at the block's edges than at its center, displaying a symmetric distribution. This emphasizes the influence of boundary effects on heterogeneity during compaction and suggests that reducing sidewall friction and height-to-diameter ratio can effectively enhance circumferential homogeneity. Note that this method is not only applicable to the block size and shape considered in this study, but can be used for any buffer blocks as long as they are orthogonally segmented.

5. Conclusions

This study focuses on the heterogeneity characterization of full-scale bentonite blocks used for HLRW buffers, providing essential insights for the design of barrier systems. Sector-shaped bentonite blocks were compacted, and their water content and dry density distributions were evaluated using the coring method to assess the homogeneity of the produced blocks. Subsequently, the blocks' hydro-mechanical behavior and microstructural features were investigated, with an emphasis on understanding their heterogeneous properties. The following principal conclusions were drawn:

(1) The water content fluctuation in the full-scale block ranges from 13.52 % to 14.14 % (initial water content of 13.9 %). In the upper layer, moisture tends to accumulate asymmetrically in the corner region on one side of the block. As the depth increases, the moisture distribution gradually shifts to a centrosymmetric pattern, with higher values at the center and lower values at the edges.
(2) The dry density in the full-scale block ranges from 1.76 g/cm^3 to 1.86 g/cm^3 (target value of 1.9 g/cm^3. In the upper layer, dry density follows a centrosymmetric distribution with lower values at the center and higher values at the edges. With increasing depth, this pattern gradually reverses. Vertically, dry density decreases from top to bottom and becomes more uniform.
(3) Compressive strength, elastic modulus, swelling pressure, and permeability are strongly correlated with dry density. Based on lab-scale results and dry density distribution, the swelling pressure is estimated to range from 5.15 MPa to 8.4 MPa, with a variation of 63.1 %, much higher than the fluctuations in dry density and water content.
(4) The pore structure heterogeneity of the block follows the order: corner regions > edge regions > center regions, and upper layer > middle layer > lower layer. Additionally, the uneven development of vertical pores caused by tensile fractures further enhances the anisotropy of the block.
(5) The distribution of dry density and water content in the upper layer is primarily influenced by gas and water expulsion during compaction. As depth increases, moisture tends to infiltrate downward from regions of lower dry density. The increase in water content enhances the compressibility of bentonite, resulting in similar distribution patterns of dry density and water content in the lower layer.
(6) The heterogeneity coefficient aligns with the variations in swelling pressure and hydraulic conductivity. Enhancing upper-block homogeneity and reducing vertical cumulative heterogeneity increase axial heterogeneity, while lowering side friction and the height-to-diameter ratio minimizes circumferential heterogeneity.

The observed heterogeneity in the physical and hydro-mechanical properties of the full-scale bentonite blocks, resulting from the compaction process, has a significant impact on the long-term performance of HLRW buffer barriers. A deeper understanding of this heterogeneity is crucial, as it not only supports the development of better buffer materials but also provides essential insights for future laboratory-scale experiments and engineering-scale numerical simulations.

CRediT authorship contribution statement

Wen-Jie Dai: Methodology, Data curation, Writing – original draft, Formal analysis, Investigation, Conceptualization. **Jing-Li Xie:** Writing – review & editing, Funding acquisition, Investigation, Methodology, Conceptualization. **Sheng-Fei Cao:** Methodology, Formal analysis, Investigation. **Yong-Gui Chen:** Writing – review & editing, Funding acquisition, Methodology.

Declaration of competing interest

The authors declare that they have no known competing financial interests or personal relationships that could have appeared to influence the work reported in this paper.

Acknowledgments

This work has been supported by the China Atomic Energy Authority (CAEA) through the Geological Disposal Program, National Natural Science Foundation of China (Grant Nos. 42125701 and 42430713), and Innovation Program of Shanghai Municipal Education Commission (Grant No. 2023ZKZD26). The authors would like to extend their most sincere gratitude to the Editors and Reviewers who provided help to edit this paper.

Appendix A. Supplementary data

Supplementary data to this article can be found online at https://doi.org/10.1016/j.jrmge.2025.06.019.

References

Asensio, L., De la Morena, G., Lopez-Vizcaino, R., Yustres, A., Navarro, V., 2018. Salinity effects on the erosion behaviour of MX-80 bentonite: a modelling approach. Appl. Clay Sci. 161, 494–504.

Bosch, J.A.A., Ferrari, A., Leupin, O., Laloui, L., 2023. Modelling the density homogenisation of a block and granular bentonite buffer upon non-isothermal saturation. Int. J. Numer. Anal. Methods GeoMech. 47 (11), 1979–2002.

Chen, Y.G., Dong, X.X., Zhang, X.D., Ye, W.M., Cui, Y.J., 2019. Cyclic thermal and saline effects on the swelling pressure of densely compacted Gaomiaozi bentonite. Eng. Geol. 255, 37–47.

Chen, Z.G., Tang, C.S., Zhu, C., Shi, B., Liu, Y.M., 2017. Compression, swelling and rebound behavior of GMZ bentonite/additive mixture under coupled hydro-mechanical condition. Eng. Geol. 221, 50–60.

Cui, L.Y., Ye, W.M., Wang, Q., Chen, Y.G., Chen, B., Cui, Y.J., 2022. Insights into gas migration in saturated GMZ bentonite using the RCP technique. Eng. Geol. 303, 106646.

Cui, L.Y., Ye, W.M., Wang, Q., Chen, Y.G., Cui, Y.J., 2023. A model for describing advective and diffusive gas transport through initially saturated bentonite with consideration of temperature. Eng. Geol. 323, 106646.

Dai, W.J., Chen, Y.G., Li, Y.C., Ye, W.M., Wang, Q., 2024. A macroscopic model for predicating stepwise crystalline swelling of montmorillonite. Comput. Geotech. 171, 106350.

Dai, W.J., Chen, Y.G., Li, Y.C., Ye, W.M., Wang, Q., Yin, Z.Y., 2025. Multiscale volumetric deformation in compacted bentonite triggered by anisotropic crystalline swelling. Eng. Geol. 346, 107888.

Davy, C.A., Skoczylas, F., Lebon, P., Dubois, T., 2009. Gas migration properties through a bentonite/argillite interface. Appl. Clay Sci. 42 (3–4), 639–648.

Delage, P., 2010. A microstructure approach to the sensitivity and compressibility of some Eastern Canada sensitive clays. Geotechnique 60 (5), 353–368.

Diaz, M.B., Kim, S.S., Lee, G.W., Kim, K.Y., Lee, C., Kim, J.S., Kim, M., 2023. Physio-mechanical and X-ray CT characterization of bentonite as sealing material in geological radioactive waste disposal. Geomech. Eng. 34 (4), 449–459.

Dutta, J., Mishra, A.K., 2015. A study on the influence of inorganic salts on the behaviour of compacted bentonites. Appl. Clay Sci. 116, 85–92.

Fan, H.H., Gao, J.N., Wu, P., Lou, Z.K., 2010. Physicochemical actions of stabilized soil with cement-based soil stabilizer. Rock Soil Mech. 31 (12), 3741–3745.

Gao, H.X., Rao, Z., Li, G.R., Liu, X.D., Liu, P.H., Li, H.H., Liu, S., Gong, Z.J., Guo, C., Ni, F.J., 2023. Evaluation of the suitability of clay rock sites for geological disposal of high-level radioactive waste in the Tamusu area, Inner Mongolia, China. J. Radioanal. Nucl. Chem. 332 (1), 47–61.

Gatabin, C., Guyot, J., Resnikow, S., Bosgiraud, J., Londe, L., Seidler, W., 2008. From bentonite powder to engineered barrier units: an industrial process. In: Proceedings of the International Conference Underground Disposal Unit Design & Emplacement Processes for a Deep Geological Repository. Prague, Czech.

Gharbieh, H., Bohner, E., Haapala, K., Salparanta, L., 2020. Bentonite buffer blocks manufactured by isostatic compression. Environ. Geotech. 7 (2), 99–109.

Gupta, A., Abed, A.A., Solowski, W.T., 2023. Identification of key thermal couplings affecting the bentonite behaviour in a deep geological nuclear waste repository. Eng. Geol. 324, 107251.

Han, Z.F., Cui, Y., Meng, Q., He, M.C., Yan, X.H., 2021. The effect of inorganic salt on the mechanical properties of montmorillonite and its mechanism: a molecular dynamics study. Chem. Phys. Lett. 781, 138982.

Holt, E., Peura, J., 2011. Buffer Component Manufacturing by Uniaxial Compression Method: Small Scale. Finland, Eurajoki. Report number: Working Report 2011-42.POSIVA.

Johannesson, L., 2019. Manufacturing of large scale buffer blocks. Uniaxial compaction of block – test made with three different bentonites. Report Number: SKB R-19-28. SKB, Stockholm, Sweden.

Joseph, C., Mibus, J., Trepte, P., Muller, C., Brendler, V., Park, D.M., Jiao, Y., Kersting, A.B., Zavarin, M., 2017. Long-term diffusion of U(VI) in bentonite: dependence on density. Sci. Total Environ. 575, 207–218.

Lee, J.O., Choi, H., Lee, J.Y., 2016. Thermal conductivity of compacted bentonite as a buffer material for a high-level radioactive waste repository. Ann. Nucl. Energy 94, 848–855.

Li, H.H., Wang, J., Mao, L., Zhao, S.W., Jia, M.L., Liu, Y.C., Huang, S.L., 2022. Safety assessment of Beishan pre-selection area for geological disposal of high-level radioactive waste in China. J. Radioanal. Nucl. Chem. 331 (6), 2573–2581.

Liu, J.F., Cao, X.L., Ni, H.Y., Zhang, K., Ma, Z.X., Ma, L.K., Pu, H., 2021. Numerical modeling of water and gas transport in compacted GMZ bentonite under constant volume condition. Geofluids 2021, 4290426.

Liu, J.F., Song, S.B., Cao, X.L., Meng, Q.B., Pu, H., Wang, Y.G., Liu, J.F., 2020. Determination of full-scale pore size distribution of Gaomiaozi bentonite and its permeability prediction. J. Rock Mech. Geotech. Eng. 12 (2), 403–413.

Liu, L., 2013. Prediction of swelling pressures of different types of bentonite in dilute solutions. Colloids Surf. A Physicochem. Eng. Asp. 434, 303–318.

Liu, Y.M., Ma, L.K., Ke, D., Cao, S.F., Xie, J.L., Zhao, X.G., Chen, L., Zhang, P.P., 2014. Design and validation of the THMC China-Mock-Up test on buffer material for HLW disposal. J. Rock Mech. Geotech. Eng. 6 (2), 119–125.

Lu, Y., Ye, W.M., Wang, Q., Chen, Y.G., 2023. Insights into anisotropic swelling pressure of compacted GMZ bentonite. Acta Geotech 18 (11), 5721–5734.

Ni, H.Y., Liu, J.F., Wang, Z.P., Sa, Q.E., Zhang, X.Y., 2024. NMR-based comparative study of gas permeability and pore structure of GMZ bentonite. Prog. Nucl. Energy 169, 105096.

Peng, J., Luo, S.M., Wang, D.F., Cao, Y.M., DeGroot, D.J., Zhang, G.P., 2022. Multiple thixotropisms of liquid limit-consistency clays unraveled by multiscale experimentation. J. Geotech. Geoenviron. Eng. 148 (1), 04021165.

Pintado, X., Kumpulainen, S., Romero, E., Lloret, A., Weber, R.C., Ferrari, A., Villar, M.V., Abed, A., Solowski, W., Heino, V., 2023. Shear strength and shear stiffness analysis of compacted Wyoming-type bentonite. Geomech. Energy Environ. 34, 100468.

Qiao, Y.F., Xiao, Y.M., Laloui, L., Ding, W.Q., He, M.C., 2019. A double-structure hydromechanical constitutive model for compacted bentonite. Comput. Geotech. 115, 103173.

Sample-Lord, K.M., Ahmed, M., Malusis, M.A., 2021. Diffusion through soil-bentonite backfill from a constructed vertical cutoff wall. Soils Found. 61 (2), 429–443.

Sanden, T., Nilsson, U., Andersson, L., 2016. Investigation of Parameters Influencing Bentonite Block Quality. Report number: SKB P-16-06. SKB, Stockholm, Sweden.

Seiphoori, A., Ferrari, A., Laloui, L., 2014. Water retention behaviour and microstructural evolution of MX-80 bentonite during wetting and drying cycles. Geotechnique 64 (9), 721–734.

Stephanie, T.-M., Greathouse, J.A., Jove-Colon, C.F., Cygan, R.T., 2015. Swelling properties of montmorillonite and beidellite clay minerals from molecular simulation: comparison of temperature, interlayer cation, and charge location effects. J. Phys. Chem. C 119 (36), 20880–20891.

Sun, W.J., Sun, D.A., Fang, L., Liu, S.Q., 2014. Soil-water characteristics of Gaomiaozi bentonite by vapour equilibrium technique. J. Rock Mech. Geotech. Eng. 6 (1), 48–54.

Tan, Y., Zhang, H.Y., Zhang, T.W., Zhang, G.C., He, D.J., Ding, Z.N., 2021. Anisotropic hydro-mechanical behavior of full-scale compacted bentonite-sand blocks. Eng. Geol. 287, 106093.

Tan, Y.Z., Hu, S.X., Li, H., Ming, H.J., Wu, J., 2024. Effect of technological voids on hydro-mechanical behavior of compacted bentonite. Environ. Earth Sci. 83 (17), 517.

Tanaka, H., Tsutsumi, A., Ohashi, T., 2014. Unloading behavior of clays measured by CRS test. Soils Found. 54 (2), 81–93.

Tanaka, Y., Watanabe, Y., 2019. Modelling the effects of test conditions on the measured swelling pressure of compacted bentonite. Soils Found. 59 (1), 136–150.

Tong, K.W., Yu, F., Dai, Z.J., Wang, H., Huang, K., Chen, S.X., Guo, J.H., 2024. Micro-level unloading behaviors of clay aggregates: a coarse-grained molecular dynamics study. Powder Technol. 443, 119922.

Ville, S., Ville, R., Keijo, H., 2020. Testing and quality control of full scale bentonite buffer block manufacturing. Posiva Working Report WR 2020-07. Posiva Oy, Eurajoki, Finland.

Wang, H., Komine, H., Gotoh, T., 2022. A swelling pressure cell for X-ray diffraction test. Geotechnique 72 (8), 675–686.

Wang, Q., Cui, Y.J., Tang, A.M., Li, X.L., Ye, W.M., 2014. Time- and density-dependent microstructure features of compacted bentonite. Soils Found. 54 (4), 657–666.

Wang, Q., Tang, A.M., Cui, Y.J., Barnichon, J.D., Ye, W.M., 2013. Investigation of the hydro-mechanical behaviour of compacted bentonite/sand mixture based on the BExM model. Comput. Geotech. 54, 46–52.

Wang, X.Y., Sun, H., Niu, F.J., 2023. Microstructure study of natural marine clay in loading and unloading processes. Eng. Geol. 327, 107363.

Wu, P., Wang, J., Ling, H., Zhou, Z.C., Santosh, M., Tang, Z.P., Sun, H.R., Gui, R.G., Duan, J.X., Li, N., Duan, X.Z., 2024. Safety assessment in the disposal of high-level radioactive wastes (HLWs): a geochemical study of uranium complexes in deep groundwater in granites from Beishan, China. J. Radioanal. Nucl. Chem. 333 (4), 1779–1791.

Xu, L., Ye, W.M., Chen, Y.G., Chen, B., Cui, Y.J., 2020. Investigation on gas permeability of compacted GMZ bentonite with consideration of variations in liquid saturation, dry density and confining pressure. J. Contam. Hydrol. 230, 103622.

Yang, Y.F., Qiao, R., Wang, Y.F., Sun, S.Y., 2021. Swelling pressure of montmorillonite with multiple water layers at elevated temperatures and water pressures: a molecular dynamics study. Appl. Clay Sci. 201, 105924.

Ye, W.M., Chen, Y.G., Chen, B., Wang, Q., Wang, J., 2010. Advances on the knowledge of the buffer/backfill properties of heavily-compacted GMZ bentonite. Eng. Geol. 116 (1–2), 12–20.

Ye, W.M., Wang, Y., Wang, Q., Chen, Y.G., Chen, B., 2020. Stress-dependent temperature effect on the swelling behavior of compacted GMZ bentonite. Bull. Eng. Geol. Environ. 79 (7), 3897–3907.

Ye, W.M., Zhu, C.M., Chen, Y.G., Chen, B., Cui, Y.J., Wang, J., 2015. Influence of salt solutions on the swelling behavior of the compacted GMZ01 bentonite. Environ. Earth Sci. 74 (1), 793–802.

Zhang, F., Xie, S.Y., Hu, D.W., Shao, J.F., Gatmiri, B., 2012. Effect of water content and structural anisotropy on mechanical property of claystone. Appl. Clay Sci. 69, 79–86.

Zhang, X.H., Chiu, Y.W., Hao, H., 2022. Dynamic tensile properties of clay bricks. Mech. Mater. 165, 104157.

Zhang, Z., Ye, W.M., Wang, Q., Chen, Y.G., 2022. Investigation on healing behavior of unsaturated GMZ bentonite pellet mixture based on compressibility. Acta Geotech 17 (10), 4461–4471.
Zhao, J.B., Zhou, Z.C., Wang, J., Ji, R.L., Zhang, M., Li, J.B., 2023. Numerical modeling of site-scale groundwater flow with stochastic parameterized hydraulic conductivity fields for geological disposal of high-level radioactive waste in China. J. Hydrol. 626, 130225.
Zhao, N.F., Ye, W.M., Chen, B., Chen, Y.G., Cui, Y.J., 2019. Investigation on unsaturated critical state and Hvorslev surface of compacted bentonite under high suction conditions. Eng. Geol. 259, 105204.
Zhou, Z.C., Wang, J., Su, R., Guo, Y.H., Li, J.B., Zhao, J.B., Zhang, M., Ji, R.L., Li, Y.N., 2023. Formation mechanism of deep groundwater at the Xinchang site of high-level radioactive waste geological disposal in China. J. Radioanal. Nucl. Chem. 332 (4), 897–905.
Zhu, J.H., Wang, Z.M., Zhang, H.Y., He, D.J., 2024. Density spatial distribution and anisotropy of full-scale bentonite-sand blocks. Constr. Build. Mater. 438, 137230.

Yong-Gui Chen is a professor in the College of Civil Engineering, Tongji University, Shanghai, China. He obtained his BEng and PhD degrees from Central South University in Hunan Province, China. He has extensive experience in research in the fields of unsaturated soils, geo-environmental engineering, urban engineering geology, and contaminated soils. He has been awarded the 14th Youth Geological Science and Technology Award of the China Geological Society, the National Science Fund for Outstanding Young Scholars (in 2014), the First Prize of the Natural Science Award of the Ministry of Education, China (in 2018), the National Science Fund for Distinguished Young Scholars (in 2021), and the Key Program of National Natural Science Foundation of China (in 2024). He has published over 150 papers in international journals and 3 industry standards in his research areas.